Electronic Supplementary Material (ESI) for ChemComm.

A Supramolecular Strategy Based on Molecular Dipole Moments for High-Quality Covalent Organic Frameworks

Laura M. Salonen,*[a] Dana D. Medina,[b] Enrique Carbó-Argibay,[a] Maarten G. Goesten,[c] Luís Mafra,[d] Noelia Guldris,[a] Julian M. Rotter,[b] Daniel G. Stroppa,[a] Carlos Rodríguez-Abreu[a]

[a]*International Iberian Nanotechnology Laboratory (INL), Av. Mestre Jose Veiga, Braga 4715-330, Portugal*

[b]*Department of Chemistry and Center for NanoScience (CeNS), Ludwig-Maximilians-University Munich (LMU), Butenandtstr. 5-11, D-81377 Munich, Germany*

[c]*Inorganic Materials Chemistry, Eindhoven University of Technology, P.O. Box 513, 5600 MB Eindhoven, The Netherlands*

[d]*CICECO-Aveiro Institute of Materials, Department of Chemistry, University of Aveiro, 3810-193 Aveiro, Portugal*

laura.salonen@inl.int

1. Abbreviations

ATR	attenuated total reflection
BET	Brunauer–Emmett–Teller
BF	bright field
Bu	butane
CC	column chromatography
COD	1,5-cyclooctadiene
COF	covalent organic framework
CP	cross-polarization
CT	contact time
d	days
DFT	density functional theory
DMAc	*N*,*N*-dimethylacetamide
DMF	*N*,*N*-dimethylformamide
EtOAc	ethyl acetate
FT-IR	Fourier transform infrared
FWHM	full width at half maximum
HAADF	high-angle annular dark field
hex	*n*-hexane
HHTP	2,3,6,7,10,11-hexahydroxytriphenylene
HR-ESI-MS	high-resolution electrospray ionization mass spectrometry
MAS	magic-angle spinning
Me	methyl
NLDFT	nonlocal density functional theory
NMR	nuclear magnetic resonance
PXRD	powder X-ray diffraction
RT	room temperature
SEM	scanning electron microscopy
SS	solid state
STEM	scanning transmission electron microscopy
TBDMS	*tert*-butyldimethylsilyl
TEM	transmission electron microscopy
*t*Bu	*tert*-butyl
TGA	thermogravimetric analysis
THF	tetrahydrofuran
TLC	thin layer chromatography
TMEDA	*N*,*N*,*N*′,*N*′-tetramethylethane-1,2-diamine
TMS	tetramethylsilane

2. Materials and Methods

Unless stated otherwise, all reactions were performed in oven-dried glassware under a positive pressure of Ar or N_2. Commercial reagents and solvents were used as received, if not otherwise specified, with the exception of pyrene, which was recrystallized prior to use from CH_2Cl_2/hexanes. Reactions were stirred magnetically and monitored by analytical thin-layer chromatography (TLC) using ALUGRAM® Xtra SIL G UV_{254} aluminium sheets from Macherey Nagel. TLC plates were visualized by exposure to ultraviolet light. Flash column chromatography was performed employing silica gel (60 Å, 40–63 µm, 230–400 mesh, Macherey Nagel).

Proton nuclear magnetic resonance (^{1}H NMR) spectra were recorded on a 400 MHz Bruker Avance II spectrometer at the NMR service of University of Minho in Braga, Portugal. Proton chemical shifts are expressed in parts per million (δ scale) and are calibrated using residual undeuterated solvent peak as an internal reference ($CDCl_3$: δ 7.26; $(CD_3)_2SO$: 2.50). Data for ^{1}H NMR spectra are reported as follows: chemical shift (δ ppm) (multiplicity, coupling constant (Hz), integration). Multiplicities are reported as follows: s = singlet, d = doublet, t = triplet, q = quartet, m = multiplet, br = broad, or combinations thereof. Carbon nuclear magnetic resonance (^{13}C NMR) spectra were recorded on a 400 MHz Bruker Avance II spectrometer. Carbon chemical shifts are expressed in parts per million (δ scale) and are referenced to the carbon resonances of the solvent ($CDCl_3$: δ 77.16; $(CD_3)_2SO$: 39.52).

Infrared (IR) spectra were recorded on a Bruker VERTEX 80v FT-IR spectrometer in transmission mode. IR data is reported in frequency of absorption (cm^{-1}).

Mass spectrometry (MS) experiments were performed on a Bruker APEX® III FTMS (ESI) instrument at Centro de Apoio Científico e Tecnolóxico á Investigación (C.A.C.T.I.) at the University of Vigo, Spain.

Small and wide angle X-ray scattering (SAXS) measurements were performed in an Anton Paar SAXSess mc2 instrument operating at 40 kV and 50 mA. Data were collected with an image plate detector. Samples were placed in a holder with Mylar windows for the measurement. All data are background corrected.

Powder X-ray diffraction (PXRD) measurements were carried out in reflection mode on a Bruker D8 Discover diffractometer with Ni-filtered Kα-radiation (λ = 1.54060 Å) and a

position-sensitive detector (LynxEye). For the simulation of the PXRD patterns the Reflex module was used (a software package implemented in MS Modeling 4.4).
Crystallite domain size was estimated from the broadening of the 100 reflection using the Scherrer formula FWHM(2θ)=$K\lambda/L\cos(\theta)$, where K = 0.9, assuming spherical particles, λ = 0.15418 nm, θ is the diffraction angle, and L the crystallite domain size. The observed FWHM was corrected for instrument broadening.

TEM and BF/HAADF-STEM imaging experiments were performed using a double (probe and image) aberration-corrected Titan Cubed Themis (FEI) electron microscope operated at 80 kV. The TEM sample was prepared by gently grinding the as-obtained **Dione-COF** into fine powder and directly transferred, without any solvent, onto a 300 mesh Cu grid covered with lacey carbon film.

Scanning electron microscopy (SEM) studies were performed using a field emission (FEG) Quanta 650 (FEI) electron microscope, operated at 3 kV and employing Everhart-Thornley detector for secondary electrons for imaging, with a working distance (WD) of ca. 10 mm. The samples for SEM were prepared by adhesion of the sample powder directly on a conductive double-sided copper tape attached to SEM pin stub.

Thermogravimetric analysis (TGA) was carried out on a TGA/DSC 1 STARe system (Mettler-Toledo). The samples were heated from 303.15 to 1173.15 K at 10 K min^{-1} under a continuous Ar flow of 20 mL min^{-1}.

Nitrogen sorption measurements were carried out using a Quantachrome Autosorb IQ2 automated analyzer. Prior to the measurements, samples were outgassed. Powder samples were outgassed by heating to 120 ºC (heating rate: 5 ºC min^{-1}, dwelling time: 720 min). Surface areas were estimated by the multipoint Brunauer–Emmett–Teller (BET) method using ASiQwin(TM) software. Pore size distribution was estimated using quenched solid density functional theory (QSDFT) for cylindrical pores (N_2 at 77 K on carbon, adsorption branch).

Solid-state NMR measurements were performed using the $^{1}H \rightarrow {}^{13}C$ Cross Polarization (CP) Magic-Angle Spinning (MAS) technique. The obtained ^{13}C spectrum was acquired on a Bruker Avance III 400 spectrometer operating at a B_0 field of 9.4 T, with ^{1}H and ^{13}C Larmor frequencies of 400.1 and 100.6 MHz, respectively, using a double-resonance 4 mm Bruker MAS probe. The ^{13}C CPMAS spectrum was acquired under the following experimental

conditions: ^{1}H 90° pulse set to 3.0 μs corresponding to a radio-frequency (rf) of ~83 kHz; the CP step was performed with a contact time (CT) of 2 ms using a 50−100% RAMP shape at the ^{1}H channel and using a 50 kHz square shape pulse on the ^{13}C channel; the recycle delay was set to 5 s. During the acquisition, a SPINAL-64 decoupling scheme was employed using a pulse length for the basic decoupling units of 5.6 μs at a rf field strength of 83 kHz.

The **Dione-COF** sample was packed into a ZrO_2 rotor using a Kel-F (4 mm) cap. A spinning rate of 12 was employed. ^{1}H and ^{13}C chemical shifts are quoted in ppm from TMS (0 ppm) and α-glycine (secondary reference, C=O at 176.03 ppm), respectively.

3. Synthetic Procedures

The synthesis of dione **2** started from the ruthenium-catalyzed oxidation of pyrene (**4**).[SI1] Pyrene-4,5-dione (**1**) was then protected using *tert*-butyldimethylsilyl chloride.[23] The following Ir-catalyzed C–H activation[23] gave **3** in 54% yield. Finally, deprotection of both protecting groups with $NaIO_4$ under acidic conditions gave boronic acid dione **2**.

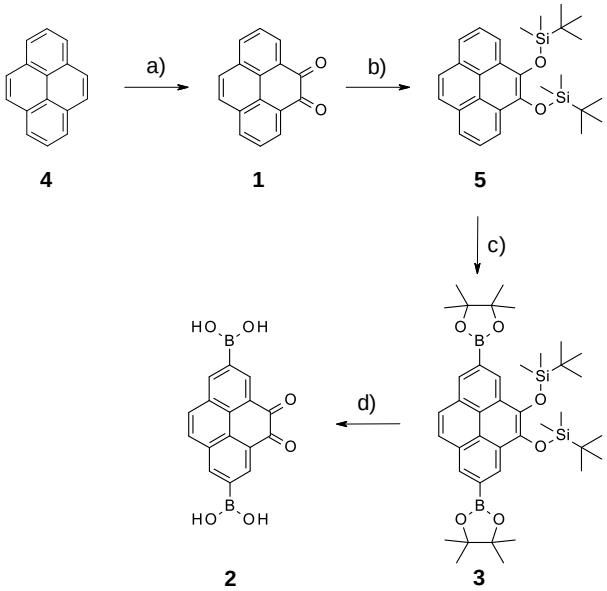

Scheme SI3.1. a) $NaIO_4$, $RuCl_3$•H_2O, CH_2Cl_2, THF, H_2O, RT, 26 h, 38%; b) Zn, TMEDA, TBDMSCl, CH_2Cl_2, RT, 68 h, 84%; c) bis(pinacolato)diboron, 4,4'-di-*tert*-butyl-2,2'-bipyridine, $[Ir(OMe)COD]_2$, cyclohexane, 105 °C, 5 d, 54%; d) $NaIO_4$, aq. 1 M HCl, THF, H_2O, air, RT, 7 d, 68%.

Pyrene-4,5-dione (1)[SI1]

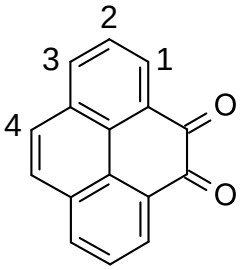

In a Schlenk flask under Ar, pyrene (**4**, 7.56 g, 37.0 mmol, 1 eq.) was dissolved in a mixture of CH_2Cl_2 (160 mL) and THF (160 mL). $NaIO_4$ (37.5 g, 175 mmol, 4.7 eq.), water (200 mL), and $RuCl_3•H_2O$ (821 mg, 3.96 mmol, 0.1 eq.) were added, and the reaction mixture was stirred at RT for 26 h. Then, the mixture was poured onto water (800 mL), and extracted with CH_2Cl_2. The organic phase was washed with water, dried over Na_2SO_4, filtrated, and evaporated to dryness. Purification by CC (SiO_2; hex/CH_2Cl_2 1:3 → CH_2Cl_2) gave **1** (3.16 g, 38%) as bright orange solid.

R_f = 0.34 (CH_2Cl_2); ^{1}H NMR (400 MHz, $CDCl_3$): 7.77 (dd, *J* = 8.0, 7.5 Hz, 2 H, H-C(2)), 7.87 (s, 2 H, H-C(4)), 8.19 (dd, *J* = 8.0, 1.3 Hz, 2 H, H-C(1) or H-C(3)), 8.51 (dd, *J* = 7.4, 1.4 Hz, 2 H, H-C(1) or H-C(3)); HR-ESI-MS: *m/z* (%): 233.05950 (100, $[M+H]^+$, calculated for $C_{16}H_9O_2^+$: 233.06025).

(7-Borono-4,5-dioxo-pyren-2-yl)boronic Acid (2)

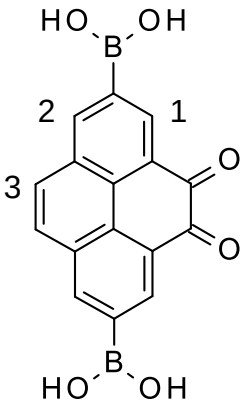

In a round-bottom flask under air, **3** (521 mg, 0.73 mmol, 1 eq.) was dissolved in THF/H_2O (15.0/4.50 mL). $NaIO_4$ (1.32 g, 6.2 mmol, 8.5 eq.) was added, and the mixture was stirred at RT for 30 min. Then, aq. 1 M HCl solution (2.38 mL) was added, and the mixture was stirred at RT for 7 d while bubbling air through the solution. The suspension was diluted with CH_2Cl_2 and water. The aq. phase was extracted with CH_2Cl_2. The org. phase was filtered, and the collected solid was combined with the aq. phase. The aq. phase was centrifuged (15 min,

4400 rpm) and orange solid was collected. The solid was suspended in water, and centrifugation was repeated. The procedure was repeated three times in total. The solid was dried under high vacuum to give **2** (160 mg, 68%) as bright orange solid.

^{1}H NMR (400 MHz, $(CD_3)_2SO+D_2O$): 8.00 (s, 2H, H-C(3)), 8.69 (d, *J* = 1.5 Hz, 2H, H-C(2)), 8.73 (d, *J* = 1.3 Hz, 2H, H-C(1)); ^{13}C NMR (100 MHz, $(CD_3)_2SO+D_2O$): 127.8, 129.0, 130.0, 131.5, 134.2, 134.4, 141.7, 180.3; IR (ATR): 3489, 3340, 1672, 1661, 1610, 1580, 1520, 1450, 1423, 1398, 1340, 1261, 1246, 1155, 1107, 1084, 1045, 947, 930, 914, 849, 829, 804, 766, 712, 665, 594, 555, 515; HR-ESI-MS: *m/z* (%): 343.05585 (100, $[M+Na]^+$, calculated for $C_{16}H_{10}B_2NaO_6^+$: 343.05612).

2,7-bis(4,4,5,5-Tetramethyl-1,3,2-dioxaborolan-2-yl)-4,5-bis(*tert*-butyldimethylsiloxy)pyrene (3)[23]

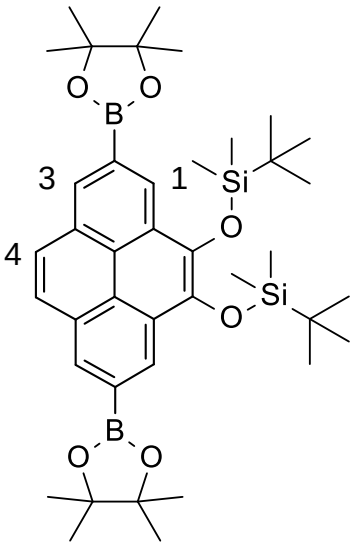

In a two-necked flask equipped with a reflux condenser under Ar, **5** (2.88 g, 6.22 mmol, 1 eq.) was dissolved in cyclohexane (150 mL), and Ar was bubbled through the solution for 20 min. Then, bis(pinacolato)diboron (3.48 g, 13.7 mmol, 2.2 eq.), 4,4'-di-*tert*-butyl-2,2'-bipyridine (152 mg, 0.57 mmol, 0.1 eq.), and $[Ir(OMe)COD]_2$ (193 mg, 0.29 mmol, 0.05 eq.) were added, and the mixture was heated to 105 °C for 5 d, cooled down, and evaporated to dryness. Purification by CC (SiO_2; hex → hex/CH_2Cl_2 9:1 → 4:1 → 3:1 → CH_2Cl_2) gave **3** (2.42 g, 54%) as off-white solid.

R_f = 0.30 (hex/EtOAc 8:1); ^{1}H NMR (400 MHz, $CDCl_3$): 0.13 (s, 12 H, Si-Me), 1.23 (s, 18 H, *t*Bu), 1.44 (s, 24 H, Me), 8.05 (s, 2 H, H-C(4)), 8.49 (dd, 2 H, *J* = 0.8 Hz, H-C(1) or H-C(3)), 8.99 (dd, 2 H, *J* = 0.8 Hz, H-C(1) or H-C(3)).

4,5-bis(*tert*-Butyldimethylsiloxy)-pyrene (5)[23]

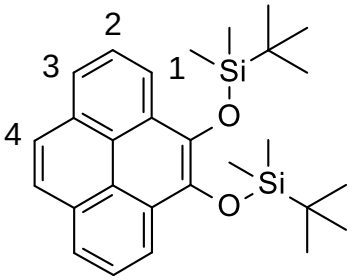

In a 2-necked flask under Ar, **1** (1.71 g, 7.36 mmol, 1 eq.) was dissolved in CH_2Cl_2 (330 mL), and Zn (7.59 g, 116 mmol, 16 eq.), *N*,*N*,*N*′,*N*′-tetramethylethane-1,2-diamine (6.20 mL, 41.4 mmol, 5.6 eq.), and *tert*-butyldimethylsilyl chloride (4.47 g, 29.7 mmol, 4.0 eq.) were added. The mixture was stirred at RT for 68 h, then filtered over a plug of silica (elution: CH_2Cl_2), and evaporated to dryness. Purification by CC (SiO_2; hex) gave **5** (2.88 g, 84%) as off-white solid. R_f = 0.26 (hex); ^{1}H NMR (400 MHz, $CDCl_3$): 0.13 (s, 12 H, Me), 1.21 (s, 18 H, *t*Bu), 7.99, (t, 2 H, *J* = 7.8 Hz, H-C(2)), 8.06 (s, 2 H, H-C(4)), 8.10 (dd, 2 H, *J* = 7.5, 1.3 Hz, H-C(1) or H-C(3)), 8.46 (dd, 2 H, *J* = 7.9, 1.1 Hz, H-C(1) or H-C(3)); ^{13}C NMR (100 MHz, $CDCl_3$): −3.3, 18.8, 26.6, 120.2, 122.0, 123.6, 125.3, 127.2, 129.7, 130.8, 138.3; HR-ESI-MS: *m/z* (%): 462.24074 (100, $[M]^+$, calculated for $C_{28}H_{38}O_2Si_2^+$: 462.24103).

4. NMR Spectra

Pyrene-4,5-dione (**1**), 400 MHz, $CDCl_3$

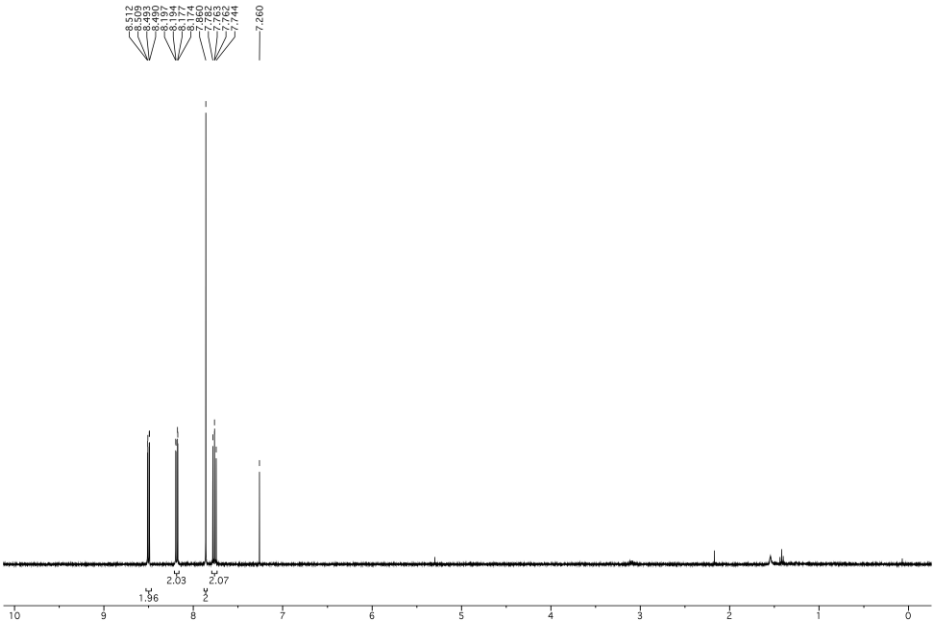

(7-Borono-4,5-dioxo-pyren-2-yl)boronic Acid (**2**), 400 MHz, $(CD_3)_2SO+D_2O$

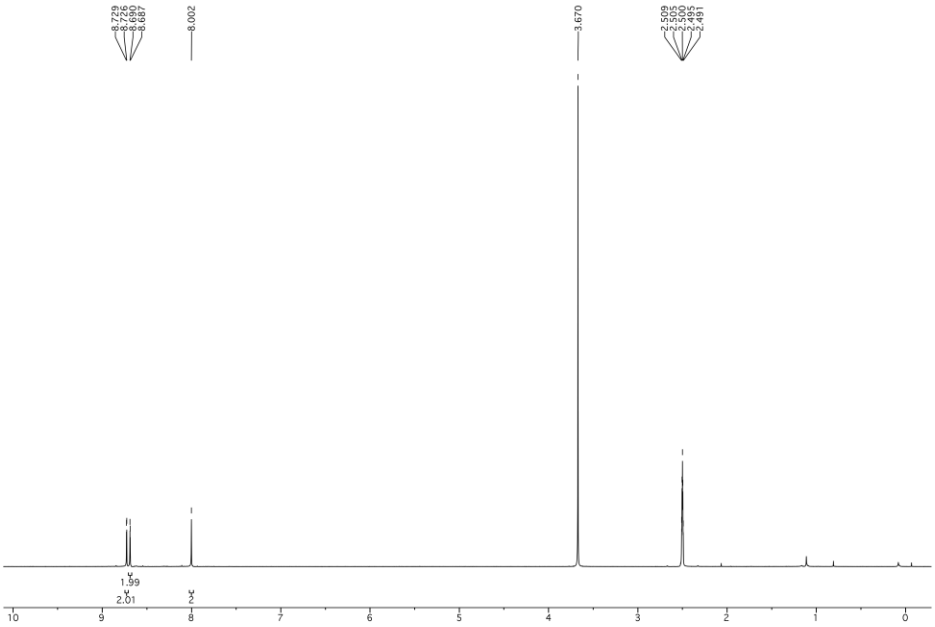

100 MHz, $(CD_3)_2SO+D_2O$

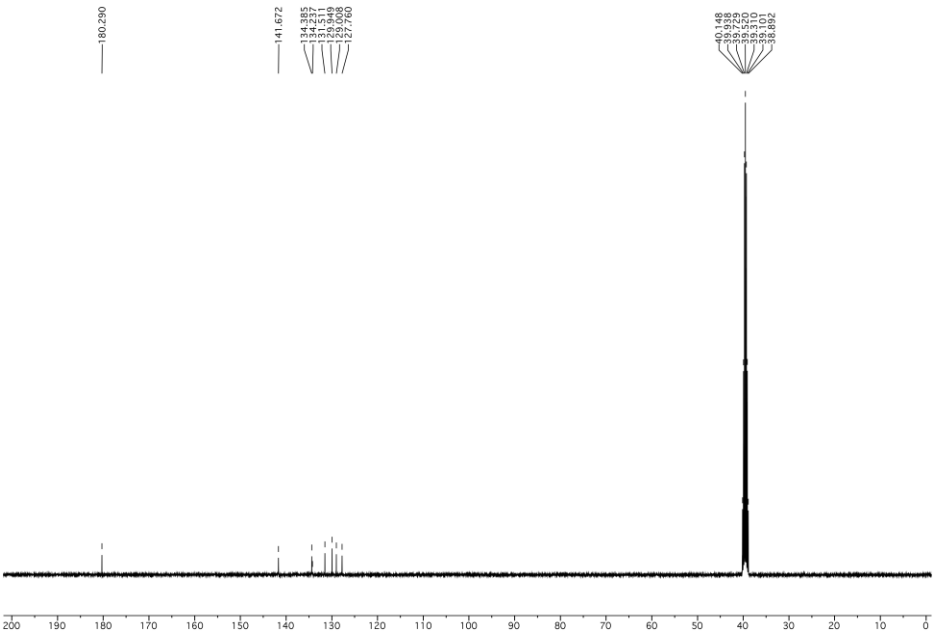

2,7-bis(4,4,5,5-Tetramethyl-1,3,2-dioxaborolan-2-yl)-4,5-bis(*tert*-butyldimethylsiloxy)pyrene (**3**), 400 MHz, $CDCl_3$

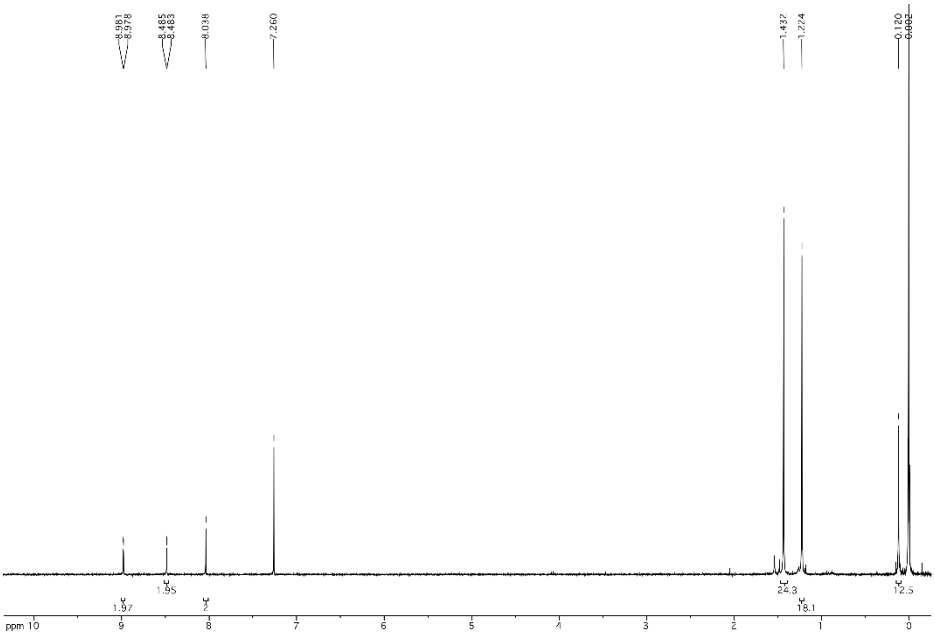

4,5-bis(*tert*-Butyldimethylsiloxy)-pyrene (**5**), 400 MHz, $CDCl_3$

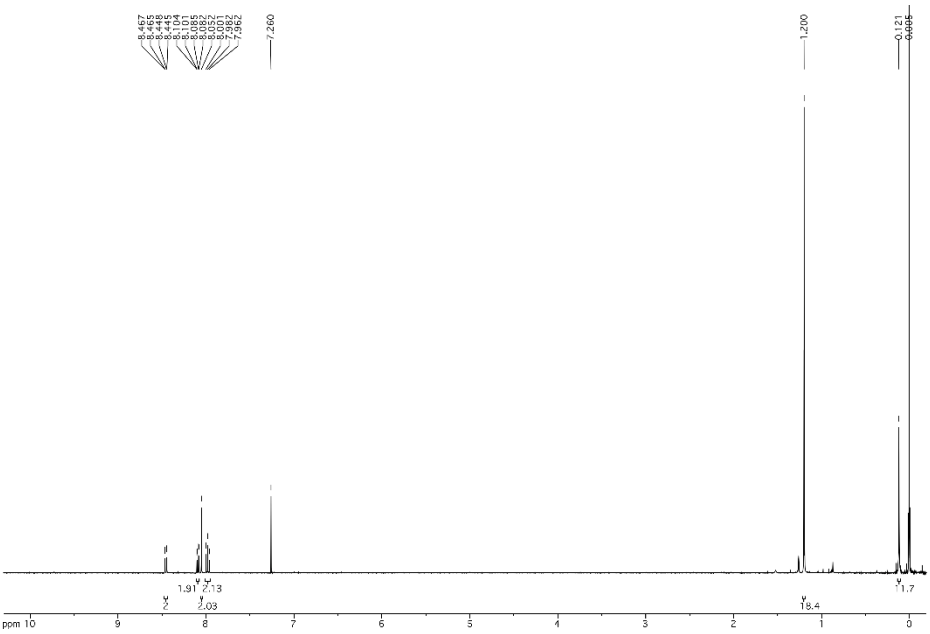

100 MHz, $CDCl_3$

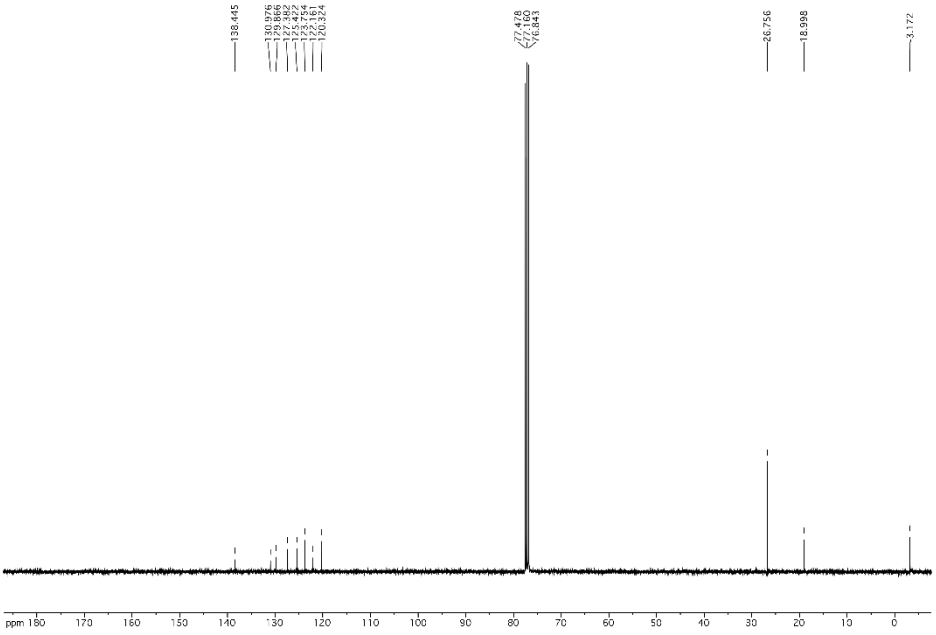

5. Studied COF Synthesis Conditions

***Dione-COF** synthesis*: To a 10 mL ampoule (Wheaton, pre-scored, borosilicate, 19 x 107 mm) were placed **2** (0.11 mmol) and HHTP hydrate (0.07 mmol), and the ampoule was flushed with Ar. A 1:1 mixture of mesitylene and *n*BuOH (4 mL), which had been degassed by three cycles of freeze-pump-thaw, was added, and the mixture sonicated for 5 min. The ampoule was immersed in a bath of liquid N_2 and sealed under vacuum. The mixture was heated in the oven at 120 °C for 7 days. The precipitate was collected by centrifugation, washed three times with anhydrous acetone, and dried under vacuum.

Yield = 32 mg (brown solid). Elemental analysis calcd (%) for ($C_{14}H_5BO_3$): C 72.48, H 2.17; found: C 69.23, H 2.42. FT-IR (ATR) = 3414 (br), 1676, 1668, 1612, 1581, 1516, 1493, 1445, 1392, 1354, 1240, 1229, 1161, 1119, 997, 978, 933, 912, 849, 835, 804, 748, 716, 675, 609, 557, 519 cm^{-1}.

Other synthesis conditions: The synthesis procedure described above for **Dione-COF** was followed, with substituting the solvent mixture with that described below in Table SI5.1. The corresponding SAXS patterns can be seen in Figure SI5.1.

Table SI5.1. Probed synthesis conditions to form **Dione-COF**.

Pattern Color	Solvents	Comments
blue	Mesitylene/*n* BuOH 1:1	
orange	Mesitylene/*n* BuOH 1:1	degassed solvents, sealed under air
light green	Mesitylene/*n* BuOH 1:1	solvents used as received, not degassed, sealed under vacuum
pink	Toluene/*n* BuOH 1:1	
red	Mesitylene/DMF 1:1	
black	Mesitylene/DMAc 1:1	
dark green	Toluene/DMAc 1:1	
navy blue	Mesitylene/Dioxane 2:1	stirred for 3 d
light purple	Mesitylene/Dioxane 1:1	stirred for 3 d

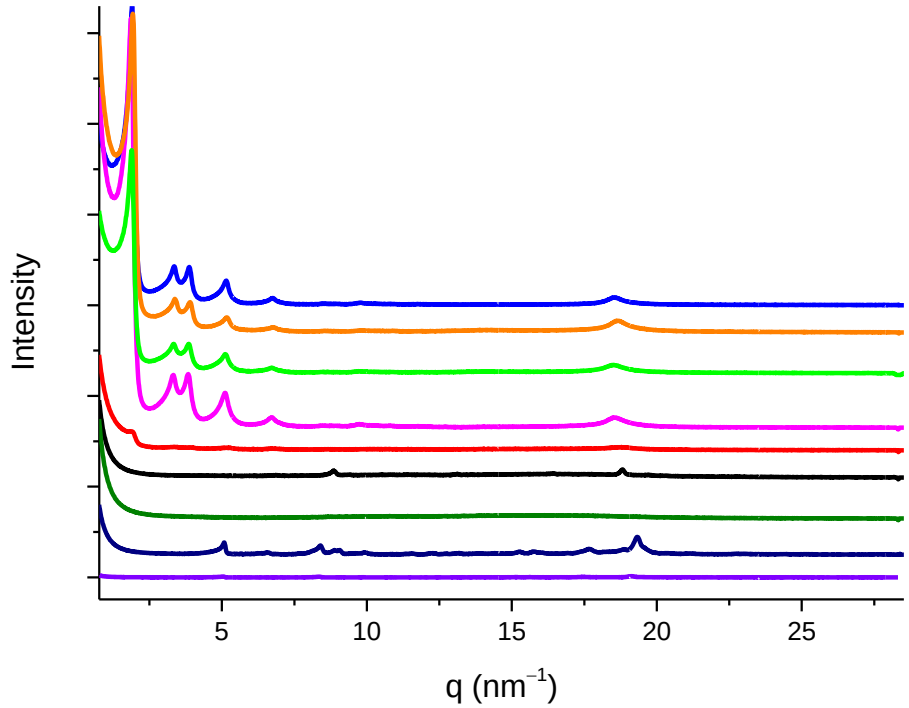

Figure SI5.1. Small angle X-ray scattering (SAXS) patterns of the samples resulting from the synthesis conditions described in the table below.

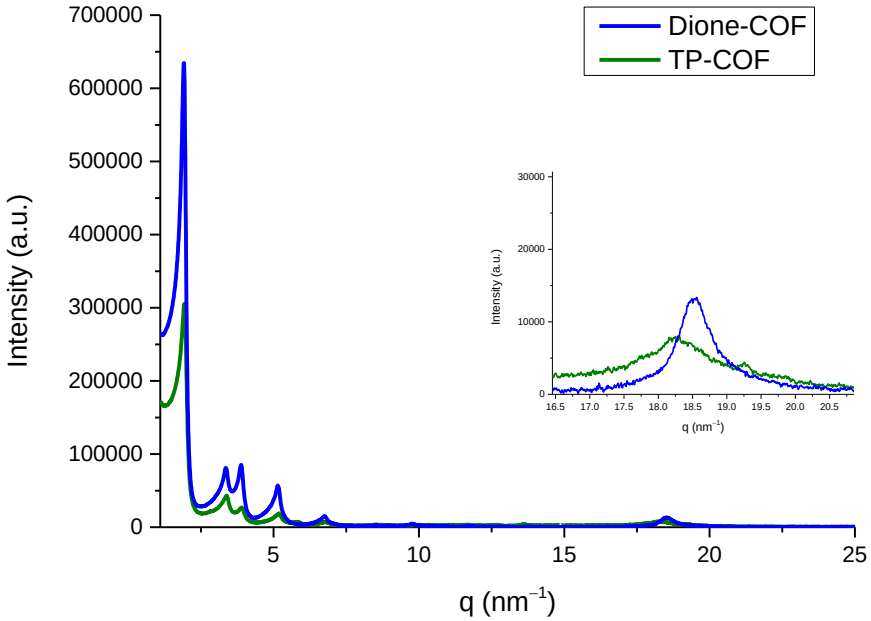

Figure SI5.2. Comparison of the SAXS patterns of **Dione-COF** and **TP-COF**, the latter prepared in-house following the procedure reported in the literature,[9a] with the inset highlighting the 001 reflection.

6. Simulation of the Crystal Structure of Dione-COF

Based on the functional groups and the geometry of **Dione-COF** precursor molecules the possible unit cells and the corresponding powder diffraction patterns were simulated. The simulated unit cells were constructed with the visualization environment of Materials Studio and the geometry of the two-dimensional layers was optimized using force field methods. Reflex package in Materials Studio software allows Pawley refinement for the simulated unit cell parameter according to the experimental PXRD. The refinement parameters R_p and R_{wp} are 5.26% and 7.25%, respectively. The simulated diffraction patterns were then confirmed by comparison to the experimental powder X-ray diffraction (PXRD) data.

Table SI6.1. Refined Crystal Data

Formula	$C_{168}O_{36}B_{12}H_{60}$
Formula weight	2784.03 g/mol
Crystal system	Hexagonal
Space group	$P6_3cm$
Unit cell dimensions	$a = b = 37.77$ Å $c = 6.92$ Å
Cell Volume	8531.40 Å^3

Table SI6.2. Fractional atomic coordinates:

Atom	Wyck.	x	y	z
C1	12d	0.70518	0.33415	0.24307
C2	12d	0.70426	0.37195	0.24307
C3	12d	0.74417	0.33620	0.24307
C4	12d	0.78004	0.37395	0.24307
C5	12d	0.77917	0.40976	0.24307
C6	12d	0.74237	0.40986	0.24307
O7	12d	0.81954	0.37991	0.24307
B8	12d	0.84338	0.42488	0.24308
O9	12d	0.81799	0.44435	0.24307
C10	12d	0.89143	0.44969	0.24309
C11	12d	0.91366	0.42892	0.24309
C12	12d	0.95674	0.45089	0.24310
C13	12d	0.97816	0.49446	0.24310
C14	12d	0.95552	0.51533	0.24310
C15	12d	0.91234	0.49272	0.24310
C16	12d	0.97859	0.42969	0.24309
C17	12d	0.97746	0.56077	0.24311
O18	12d	0.74827	0.30987	0.24307
H19	12d	0.74509	0.43972	0.24307
H20	12d	0.89748	0.39557	0.24309
H21	12d	0.89501	0.50871	0.24310
H22	12d	0.96249	0.39638	0.24309
H23	12d	0.95864	0.57946	0.24312

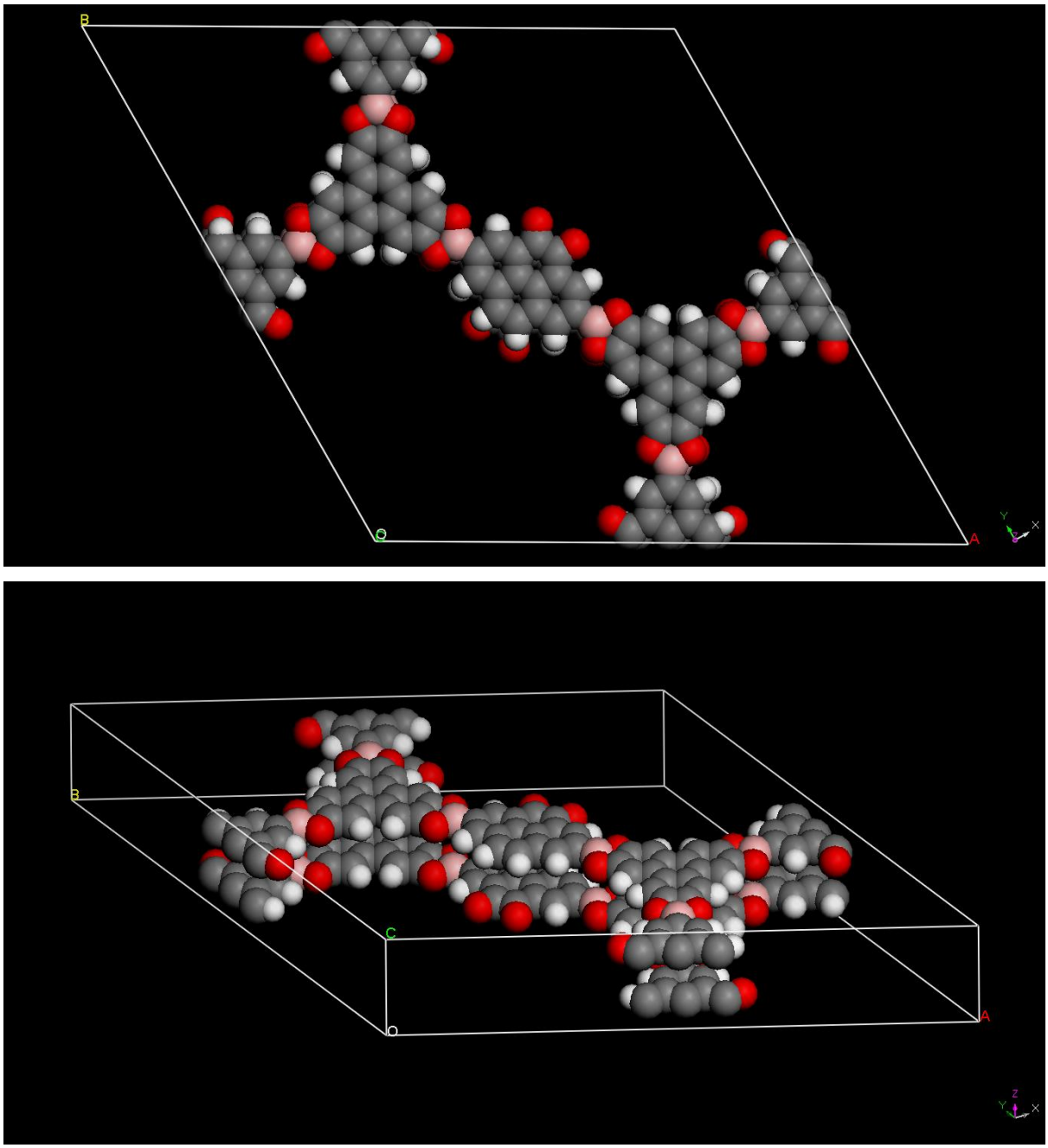

Figure SI6.1. Simulation of the crystal unit cell calculated in an eclipsed arrangement in the $P6_3cm$ space group. **Top**: top view on *ab*-plane, **bottom**: view along *b*-axis with an interlayer distance of 3.45 Å.

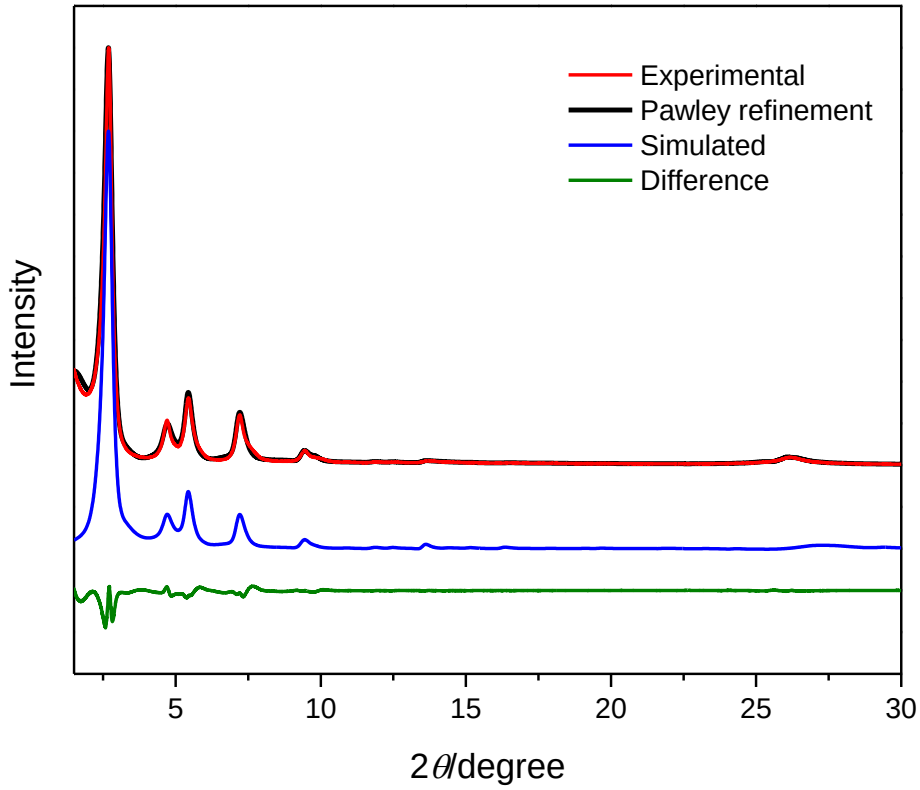

Figure SI6.2. Experimentally obtained PXRD pattern (red), Pawley refinement (black) simulated patterns obtained by the Reflex module in MS Studio, based on an eclipsed AA arrangement in (blue), and a difference plot of the experimental and simulated pattern (green).

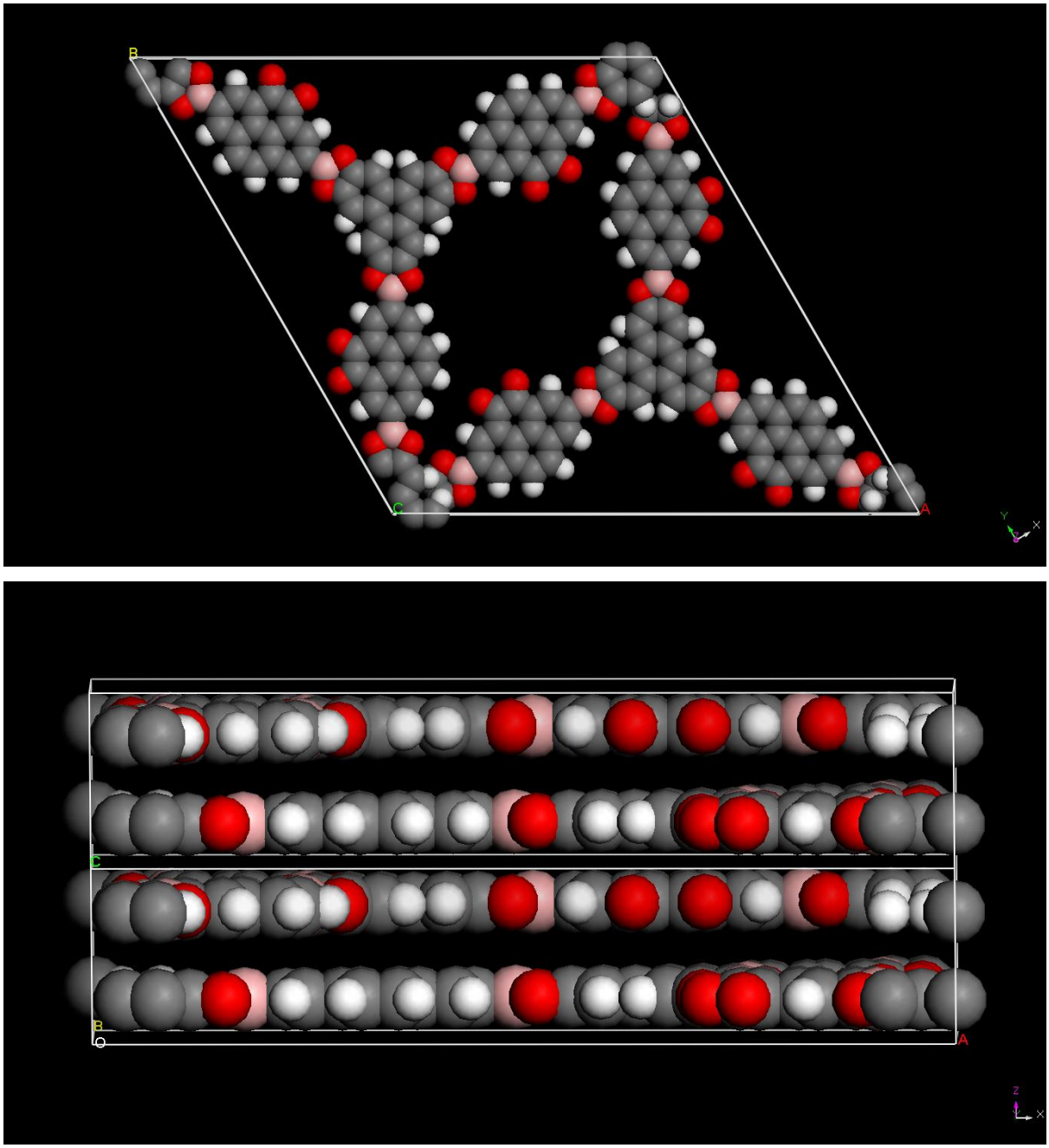

Figure SI6.3. Simulation of the **Dione-COF** unit cell calculated in an AB staggered layer arrangement (space group $P6_3$). **Top**: view on ab-plane; the pore size and the internal surface are significantly smaller than the experimental data, **bottom**: view along c-axis: doubling of the sheets leads to a larger interlayer distance.

In addition, we simulated the diffraction patterns of different unit cells with AA layer stacking arrangements.

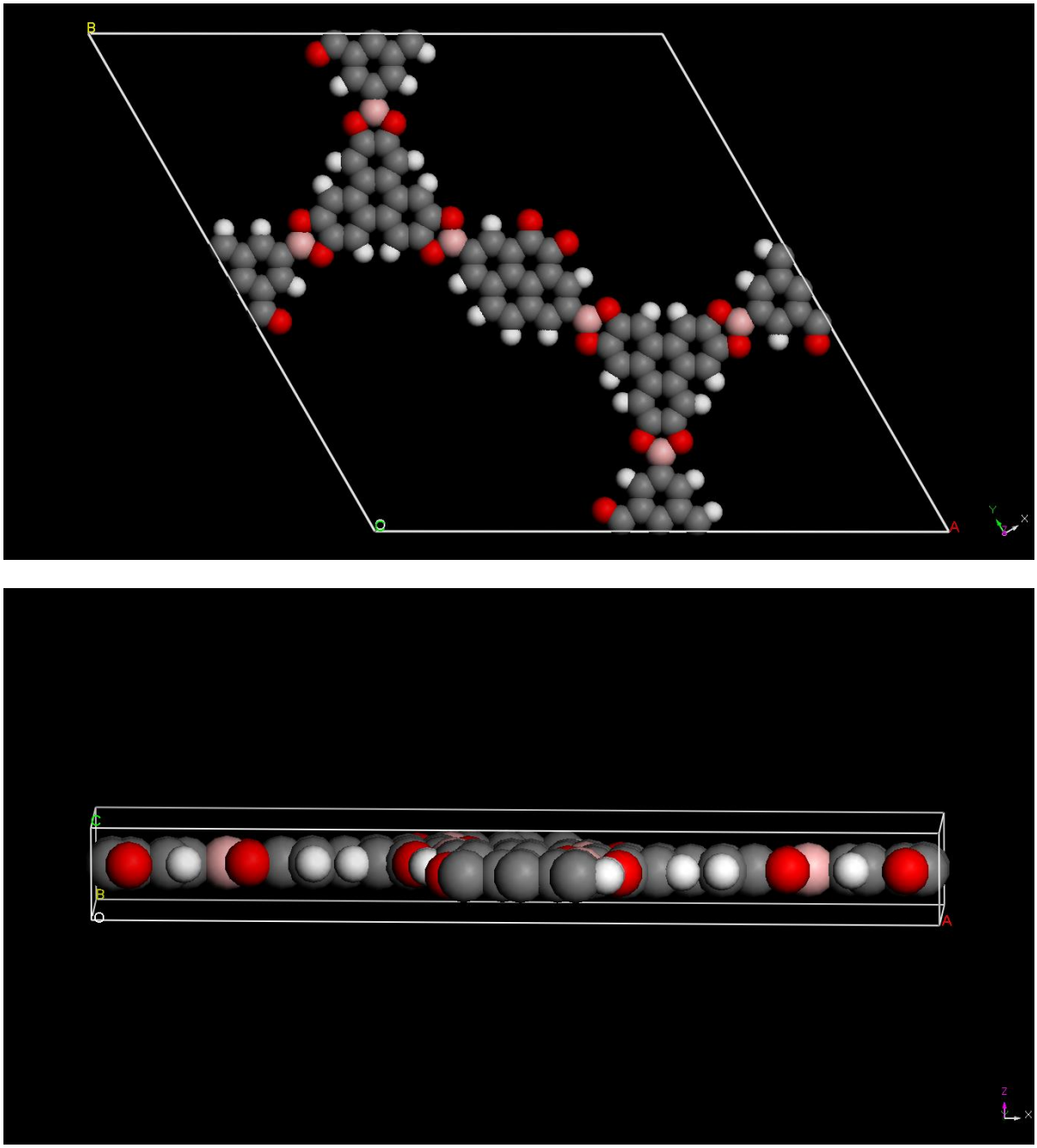

Figure SI6.4. Simulation of the crystal unit cell calculated in an eclipsed arrangement in the *P*6-2m space group. **Top**: top view on *ab*-plane, **bottom**: view along *b*-axis with an interlayer distance (along *c*) of 3.53 Å.

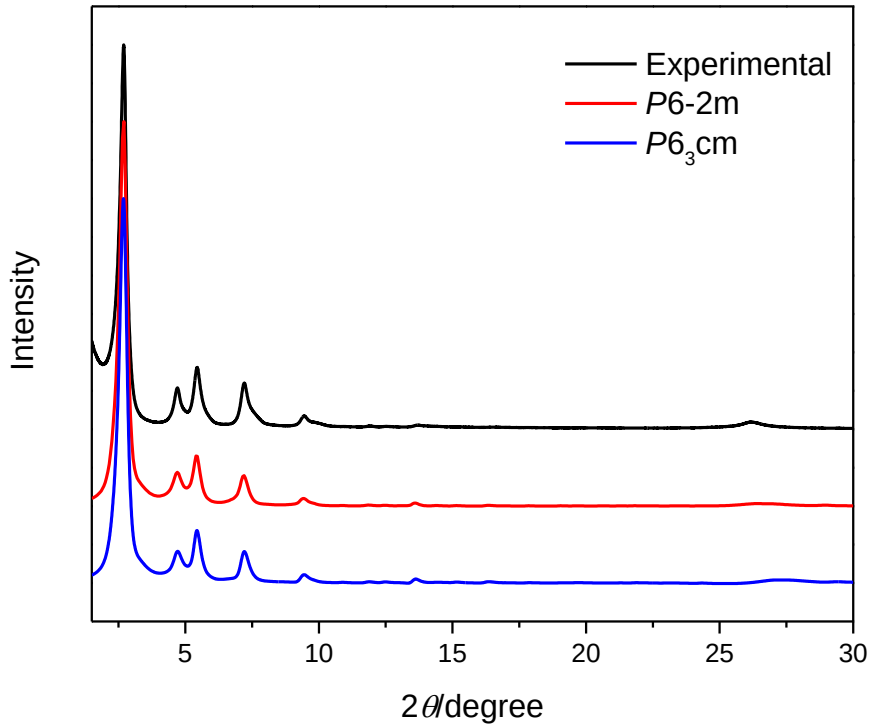

Figure SI6.5. Experimentally obtained PXRD pattern (black), simulated patterns obtained by the Reflex module in MS Studio, based on an eclipsed AA arrangement in the *P*6-2m space group (red) and in the *P*6$_3$cm space group (blue). On the level of theory on which the PXRD pattern simulations are performed, using Reflex package in Materials Studio software, and due to the broadness of the PXRD signals, there is no significant difference between the patterns calculated for the parallel and antiparallel arrangement of the molecules.

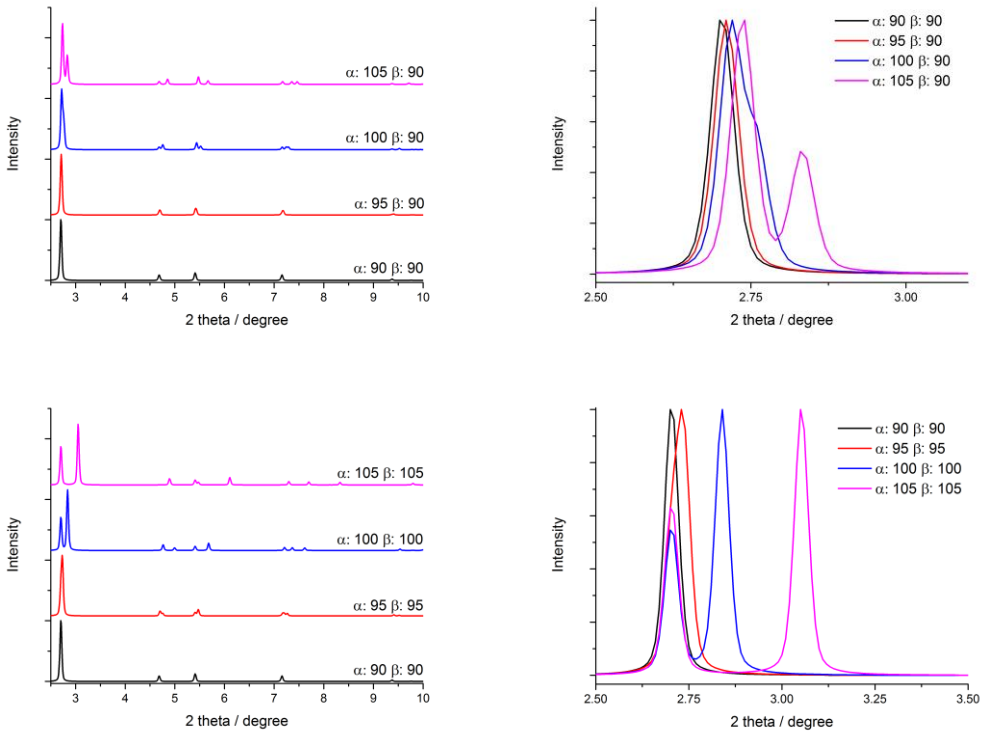

Figure SI6.6. Simulated shifts in PXRD reflection positions upon moving the layers on top of each other. α,β: 90° corresponds to the refined cell parameters from the experimental PXRD data and an eclipsed (AA) packing arrangement as for *P*6-2m symmetry. Slipping of the layers was simulated by changing one (top) or both (bottom) of the 90° angles of the hexagonal cell in 5° steps up to 105°, resulting in a maximal layer offset of 15°. When only one angle is changed, a shift to smaller 2θ can be observed and a peak splitting occurs at higher offset angles. If both angles are changed, the same effect can be observed in a more drastic manner. The experimental peak positions are best reproduced by the α,β: 90°, suggesting that a slipping of layers does not occur in this system.

7. Thermogravimetric Analysis

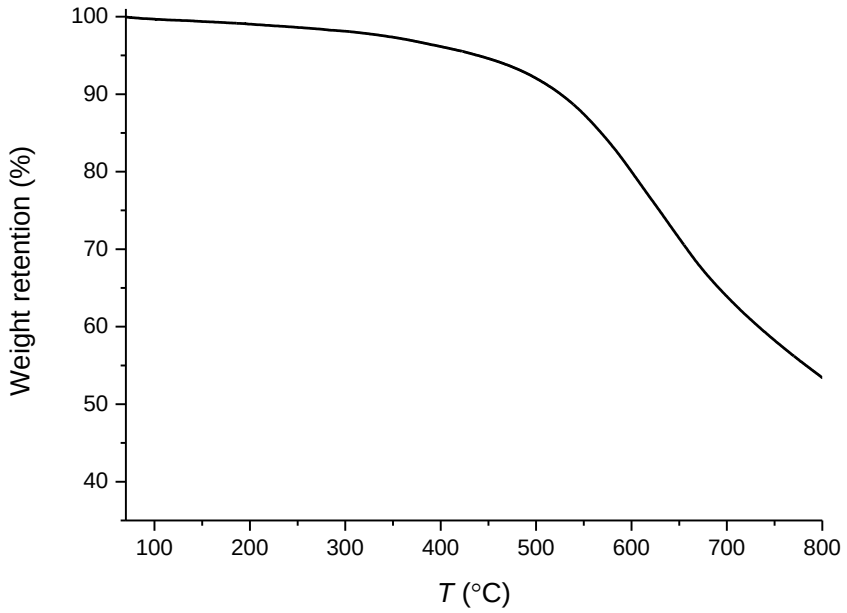

Figure SI7.1. TGA profile of **Dione-COF**.

8. FT-IR Spectra

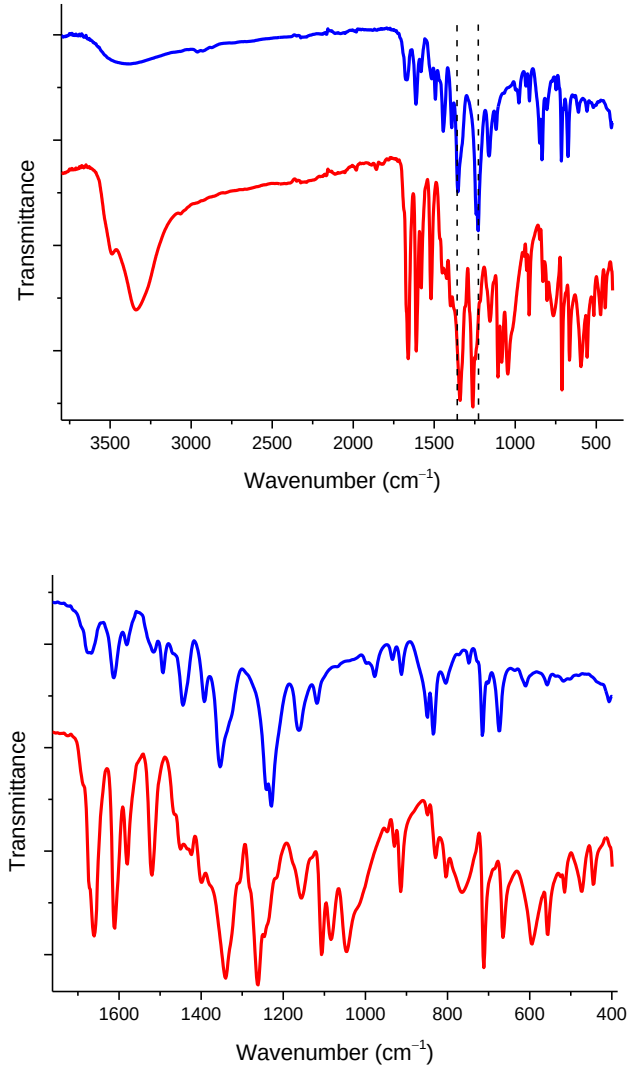

Figure SI8.1. Top: FT-IR spectra of dione building block **2** (red) and **Dione-COF** (blue), highlighting the bands characteristic[25] for B–C and C–O stretching of boronic esters. Additionally, compared to the IR spectra of monomer **2**, the considerable attenuation of the O–H band at 3100–3500 cm^{-1} in the case of **Dione-COF** indicates boronic ester formation. **Bottom**: Overlay of zoomed spectra.

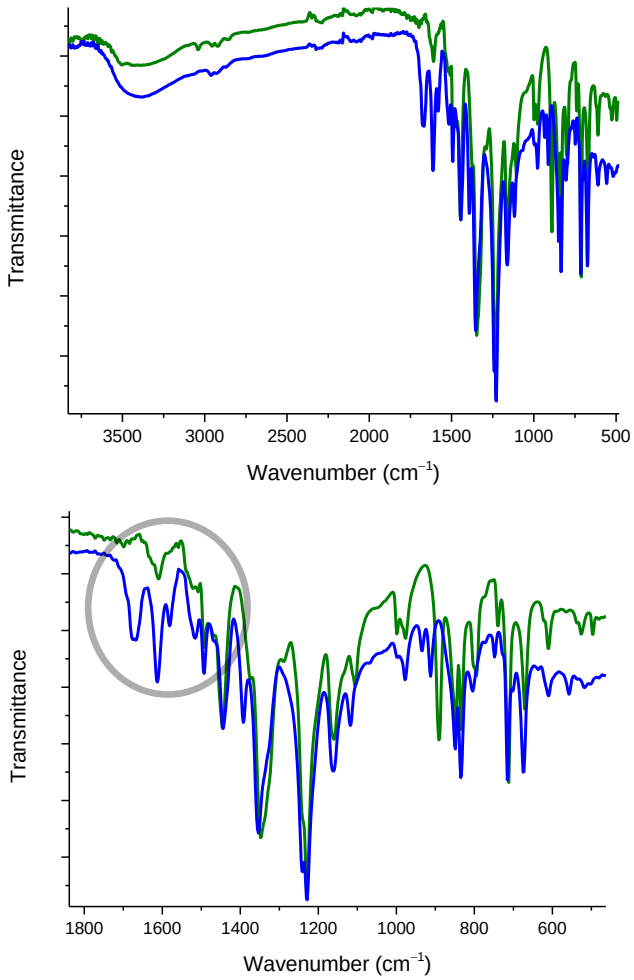

Figure SI8.2. Overlay of FT-IR spectra of **Dione-COF** (blue) and **TP-COF**[9a] (dark green, synthesized in house following the reported procedure): full spectra (left), and a zoom (right) highlighting the differences in the spectra.

9. Solid-State NMR

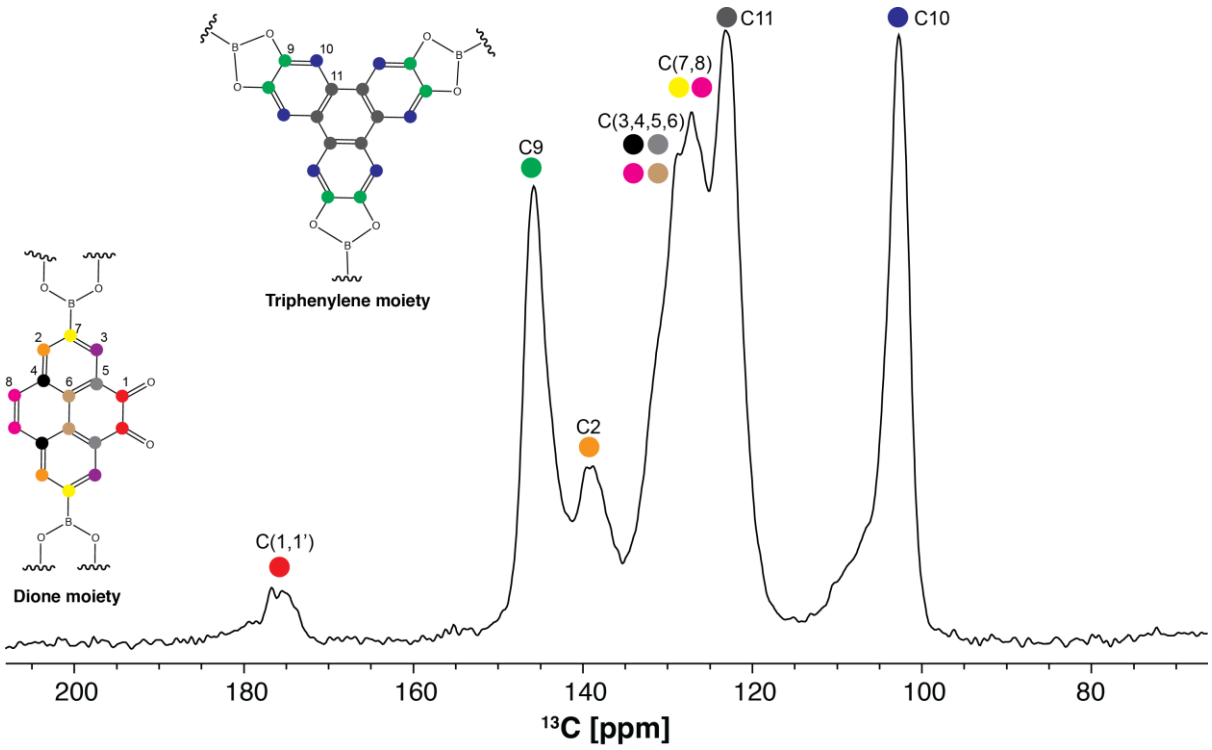

Figure SI9.1. ^{13}C CPMAS spectrum of **Dione-COF**. The molecular fragments forming the crystal packing of the material are depicted using a color code to facilitate the visualization of the carbon position and the ^{13}C resonance position. Calculated and experimental ^{13}C chemical shifts are compared in Table SI9.1 to aid in the resonance assignment task.

Computational details: The calculation of NMR chemical shieldings was performed within the framework of DFT, using the plane wave pseudopotential formalism and the PBE exchange correlation functional.[SI2] All calculations were performed with CASTEP code[SI3] using a Linux workstation with 64 Gb RAM (2133 MHz ECC DDR4); dual socket Intel Xeon processor E5−2650 v 3 family @ 2 GHz using 16 cores with 2 threads in each core (hyper-threading); QPI up to 9.6 GT/s, and employing ultrasoft pseudopotentials calculated on the fly. The gauge including projector augmented wave (GIPAW) approach of Pickard *et al.*[SI4,SI5] was employed, which allows chemical shifts to be calculated with an all-electron accuracy within the pseudopotential framework.

The starting structure model of **Dione-COF** was obtained from the simulated crystal structure (see Section 6), as described above. An initial optimization of all atom positions was conducted until reaching full convergence using LBFGS geometry optimization employing a plane wave basis set cutoff of 400 eV and a 1 × 1 × 2 Monkhorst−Pack (MP) k-point grid for SCF calculations. A total energy atom convergence tolerance of 1 × 10^{-8} eV was used; all other

CASTEP geometry convergence criteria were set to their default values. After full geometry optimization, calculation of ^{13}C chemical shieldings was performed using the same basis set cutoff and MP grid indicated above. Conversion of the calculated isotropic chemical shieldings (σ_{iso}) into the corresponding isotropic chemical shifts (δ_{iso}) was performed according to the formula (see Table SI9.1):

$\delta_{iso} = (\sigma_{iso} - \sigma_{ref})/m$

where σ_{ref} and m are the y-intercept and slope, respectively, resulting from a linear regression obtained by plotting σ_{iso} against δ_{iso} (Figure SI9.2).

Table SI9.1. Experimental and calculated ^{13}C chemical chifts (δ_{iso}) of **Dione-COF**.

Carbon label[a]	**exp.** δ_{iso} / ppm	**calc.** σ_{iso} / ppm[b]	**calc.** δ_{iso} / ppm[b]
C1	176.7	–7.0	176.3
C1'[c]	175.5	–6.2	175.5
C2	139.5	30.0	141.0
C3	n/a	37.9	133.5
C(4, 5, 6)[d]	129.0	44.8	127.0
C(7, 8)[d]	126.5	46.8	125.0
C9	146.0	24.2	146.6
C10	102.7	68.5	104.4
C11	123.2	50.3	121.7

[a]Labels are depicted in Figure SI9.1. Although much more chemical shift (CS) values were obtained from calculations than the ones shown in the table, only nine ^{13}C CS values were compared, as these were the only ones that could be observed from the experimental spectrum. [b]All calculated CS values are shown as average values of the various chemically equivalent carbons modeled. As there are 168 carbons present, for the sake of simplicity, only the average CS for each carbon located at the positions corresponding to the labels was considered. [c]The prime means that it was possible to unequivocally distinguish, experimentally, two chemically equivalent carbon environments (1 and 1') and therefore their average CS value was not taken in this case. [d]Whenever the ^{13}C CS values were too close to be distinguished experimentally, those CSs were merged and only their average was considered.

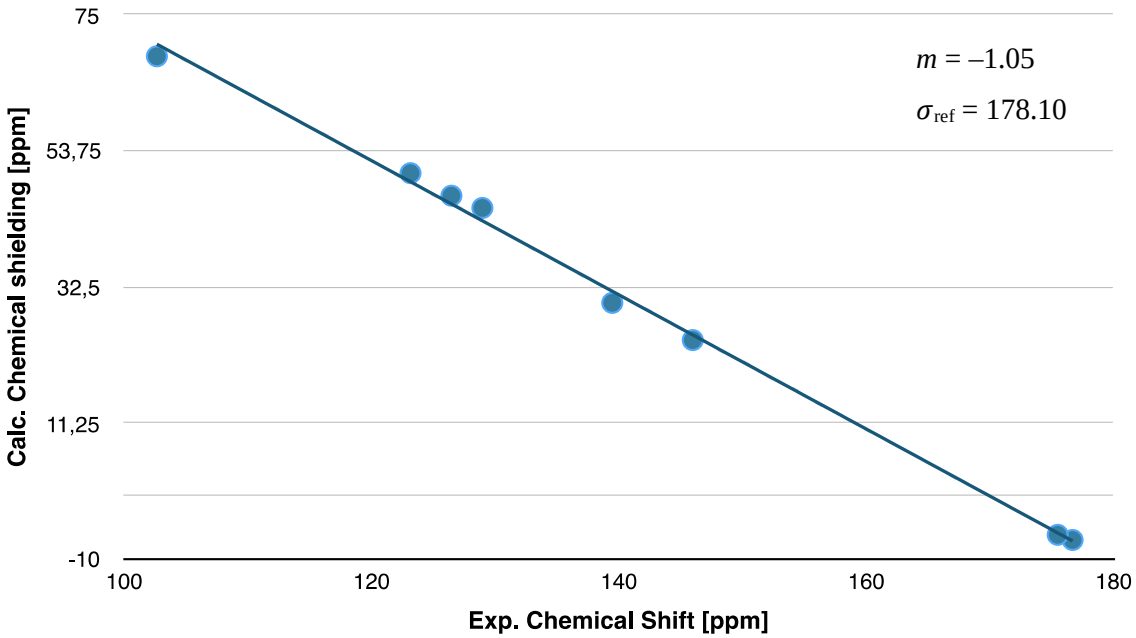

Figure SI9.2. GIPAW calculated chemical shieldings *versus* measured chemical shifts for ^{13}C resonances of **Dione-COF** along with the corresponding conversion parameters (*m* and σ_{ref}) to convert chemical shieldings (σ_{iso}) into chemical shifts (δ_{iso}) using the expression $\delta_{iso} = (\sigma_{iso}–\sigma_{ref})/m$.

10. SEM Imaging

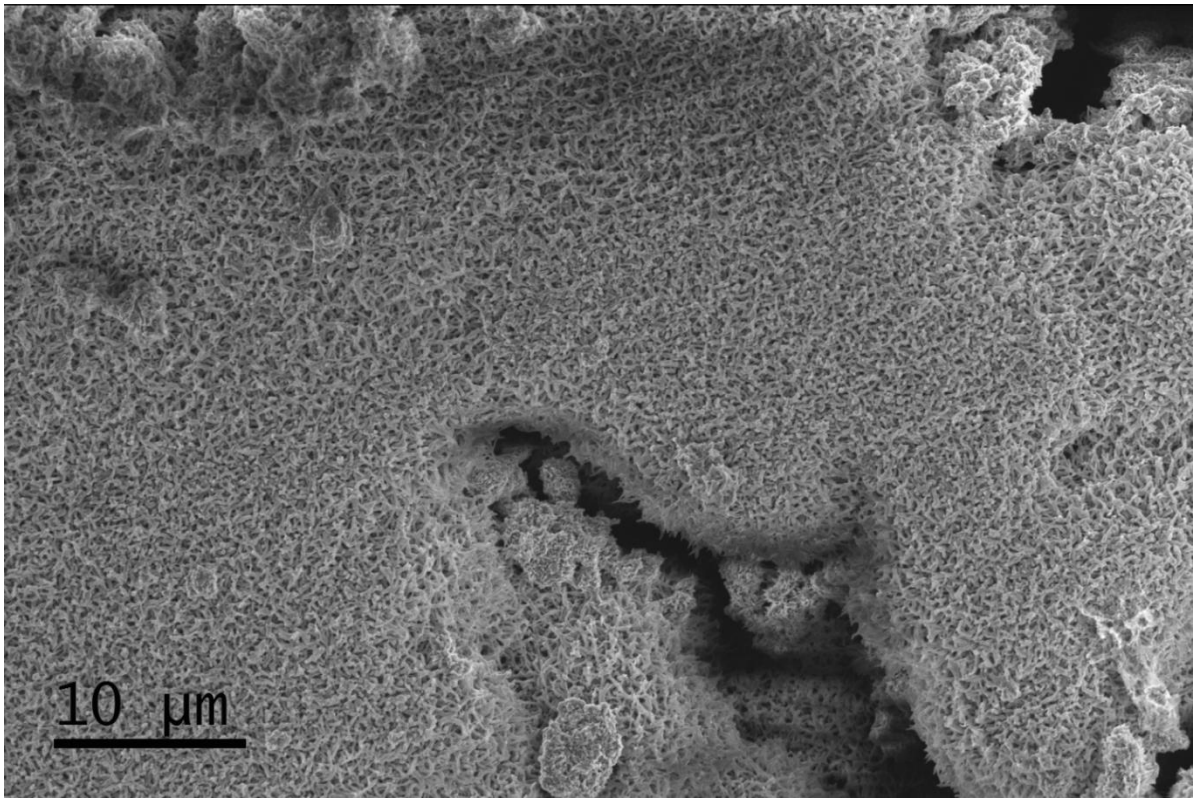

Figure SI10.1. SEM image (secondary electrons detector at 3 kV) at very low magnification of synthesized **Dione-COF**, highlighting the uniformity of the formed microstructures.

11. TEM/STEM imaging

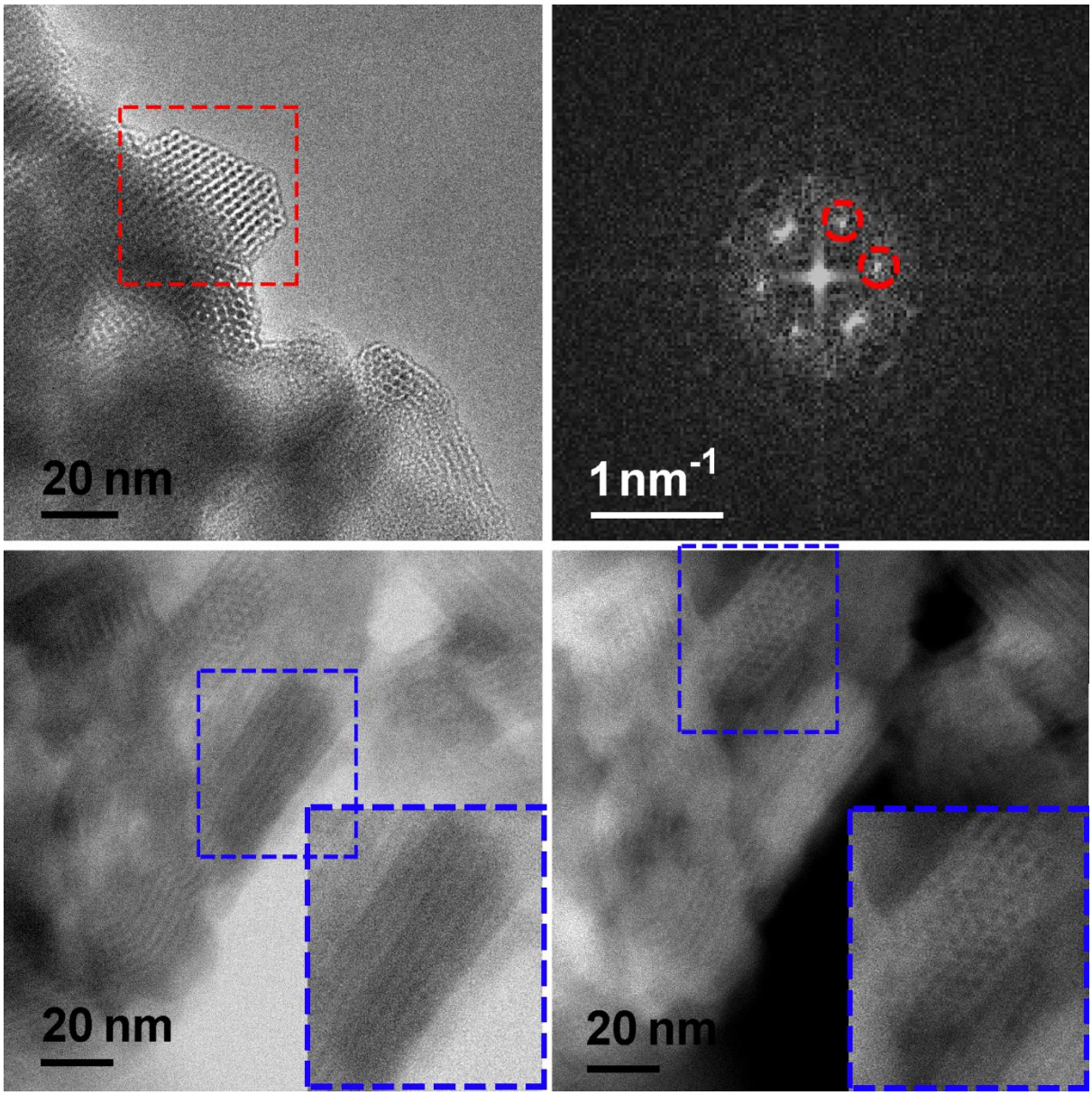

Figure SI11.1. Top left: TEM image showing different regions with the typical porous structure of **Dione-COF**. The inset highlights a region oriented in the <001> zone axis, in which the pores present a hexagonal symmetry. **Top right**: Fourier Transform of the highlighted region on previous TEM image, confirming the **Dione-COF** crystallinity and the hexagonal symmetry of the spatial frequencies present on the viewing zone axis. The periodicity extracted from reciprocal space measurements refers to the pore spacing, evaluated here 2.4±0.2 nm (0.43–0.42 nm^{-1}). One hypothesis to justify the deviation with respect to the crystallographic structure determined by XRD is shrinkage due to the TEM ultra-high vacuum level.

Bottom: Bright field (left) and high-angle annular dark field (right) STEM images displaying fringes (lateral view of the longitudinal axis of the pores, see scheme below) and the typical porous structure of **Dione-COF**, respectively.

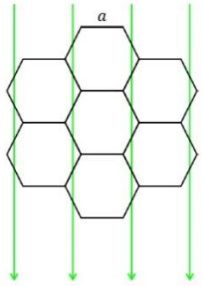

12. Porosimetry

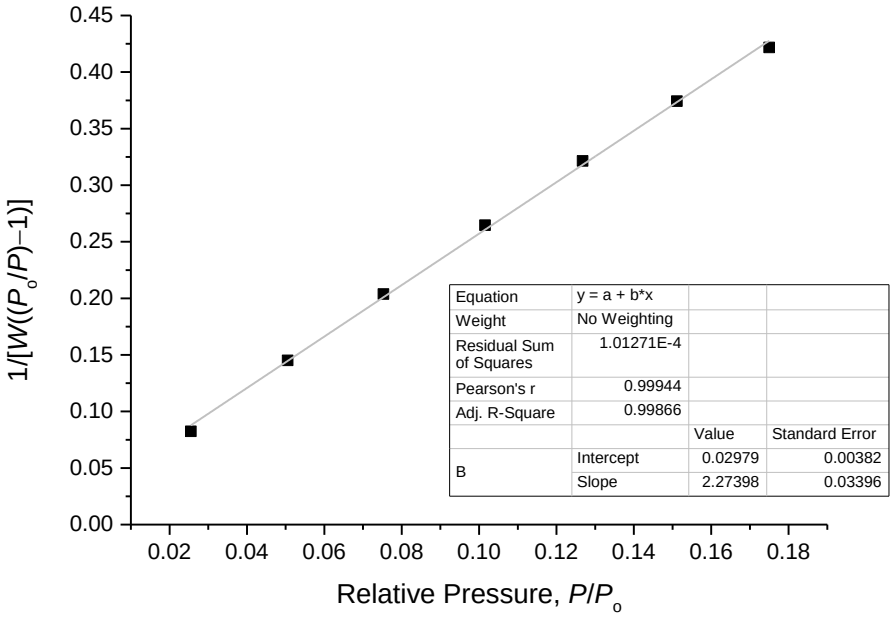

Figure SI12.1. Multi-point BET plot and linear fit of **Dione-COF**.

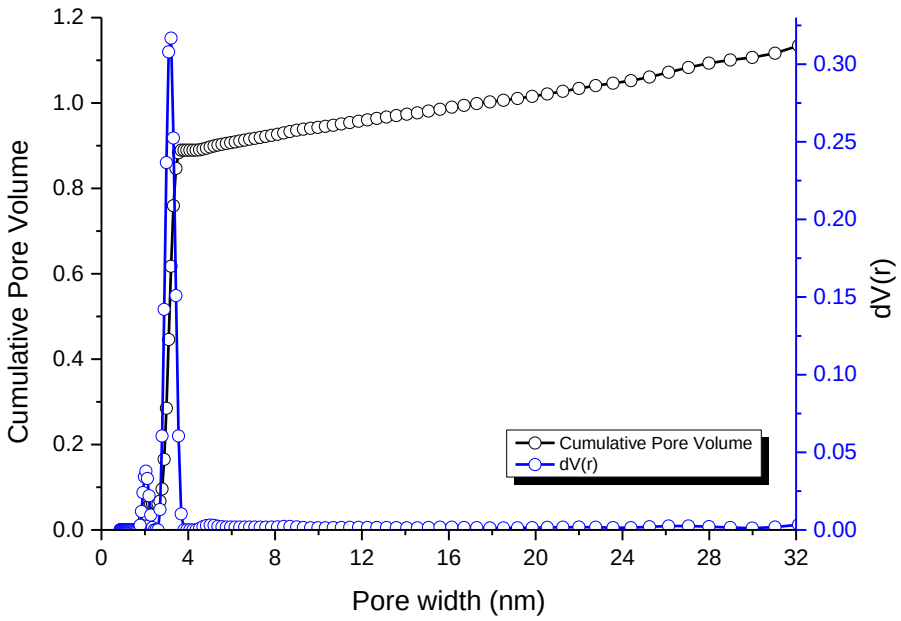

Figure SI12.2. Pore size distribution (blue) and cumulative pore volume (black) profiles.

13. Interaction Energy Calculations

All calculations were performed using the generalized gradient approximation (GGA) of DFT using the Amsterdam Density Functional (ADF) program.[SI6] The numerical integration was performed using a refined version of the fuzzy cells integration scheme developed by Becke.[SI7,SI8] The molecular orbitals (MOs) were expanded in a large uncontracted set of Slater type orbitals (STOs) containing diffuse functions, of triple-ζ quality for all atoms, augmented with two sets of polarization functions (TZ2P).

The use of exact density, rather than fitted density, in calculation of the exchange-correlation potential, was required to remove all imaginary frequencies from harmonic analysis of the geometrically optimized systems.

All energies and geometries were calculated using the generalized gradient approximation (GGA) of DFT at the BLYP level of theory. GGA proceeds from the local density approximation (LDA) where exchange is described by Slater's X_α potential and correlation is treated in the Vosko–Wilk–Nusair (VWN) parametrization, which is augmented with nonlocal corrections to exchange according to Becke and correlations according to Perdew added self-consistently.

The core shells of all atoms were treated by the frozen-core (FC) approximation.[SI9] For all calculations, relativistic effects were accounted for by Zeroth-Order Regular Approximation (ZORA),[SI10] and dispersion was taken into account by Grimme's latest correction, D3.[SI11] The energy associated with deformation of the separate fragments in forming the dimer, ΔE_{strain} was estimated to be negligible, *i.e.* 0.3–0.4 kcal mol^{-1}, for all cases.

Energy Decomposition Analysis

ΔE_{oi} = orbital interactions; ΔE_{Pauli} = Pauli repulsion between electrons of parallel spin; ΔV_{elstat} = electrostatic interaction, ΔE_{disp} = dispersion interaction; ΔE_{int} = total interaction energy

Antiparallel dipole alignment

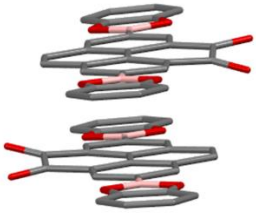

ΔE_{oi} = –11.4 kcal mol^{-1}

ΔE_{Pauli} = +55.9 kcal mol^{-1}

ΔV_{elstat} = –23.7 kcal mol^{-1}

ΔE_{disp} = –60.3 kcal mol^{-1}

ΔE_{tot} = –39.5 kcal mol^{-1}

Parallel dipole alignment

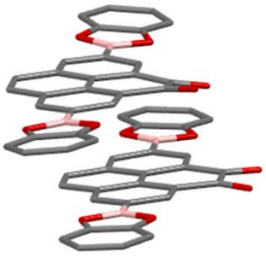

ΔE_{oi} = –11.0 kcal mol^{-1}

ΔE_{Pauli} = +52.6 kcal mol^{-1}

ΔV_{elstat} = –19.0 kcal mol^{-1}

ΔE_{disp} = –56.6 kcal mol^{-1}

ΔE_{tot} = –34.0 kcal mol^{-1}

No dipole

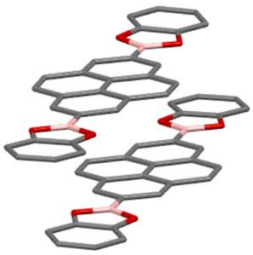

ΔE_{oi} = –8.7 kcal mol^{-1}

ΔE_{Pauli} = +49.1 kcal mol^{-1}

ΔV_{elstat} = –18.6 kcal mol^{-1}

ΔE_{disp} = –54.0 kcal mol^{-1}

ΔE_{tot} = –32.2 kcal mol^{-1}

14. References

SI1. G. Venkataramana, P. Dongare, L. N. Dawe, D. W. Thompson, Y. Zhao, G. J. Bodwell, *Org. Lett.* **2011**, *13*, 2240–2243.

SI2. J. P. Perdew, K. Burke, M. Ernzerhof, *Phys. Rev. Lett*. **1996**, *77*, 3865−3868.

SI3. S. J. Clark, M. D. Segall, C. J. Pickard, P. J. Hasnip, M. I. J. Probert, K. Refson, M. C. Payne, *Z. Kristallogr*. **2005**, *220*, 567−570.

SI4. C. J. Pickard, F. Mauri, *Phys. Rev. B* **2001**, *63*, 245101.

SI5. J. R. Yates, C. J. Pickard, F. Mauri, *Phys. Rev. B* **2007**, *76*, 024401.

SI6. www.scm.com

SI7. A. D. Becke, *J. Chem. Phys.* **1988**, *88*, 2547–2553.

SI8. M. Franchini, P. H. T. Philipsen, L. Visscher, *J. Comput. Chem.* **2013**, *34*, 1819–1827.

SI9. E. J. Baerends, D. E. Ellis, P. Ros, *Chem. Phys.* **1973**, *2*, 41–51.

SI10. E. Van Lenthe, J. G. Snijders, E. J. Baerends, *J. Chem. Phys.* **1996**, *105*, 6505–6516.

SI11. S. Grimme, J. Antony, S. Ehrlich, H. Krieg, *J. Chem. Phys.* **2010**, *132*, 154104–154123.